Korean J. Chem. Eng., 40(6), 1457-1473 (2023)
DOI: 10.1007/s11814-023-1391-5

pISSN: 0256-1115
eISSN: 1975-7220

A new ternary mixed-matrix membrane (PEBAX/PEG/MgO) to enhance CO_2/CH_4 and CO_2/N_2 separation efficiency

Navid Azizi*,†, Omid Jahanmahin, Reza Homayoon*, and Mohammad Khajouei*****

*Department of Chemical Engineering, Shiraz Branch, Islamic Azad University, Shiraz, Iran
**Department of Chemical Engineering, Pennsylvania State University, University Park, PA16802, USA
***Nanotechnology Research Institute, School of Chemical Engineering, Babol (Noshirvani) University of Technology, Babol, Iran

(*Received 22 July 2022 • Revised 8 December 2022 • Accepted 29 December 2022*)

Abstract−Mixed-matrix membranes (MMMs) composed of suitable CO_2-philic polymers and fillers can be attractive candidates for CO_2/CH_4 and CO_2/N_2 separation due to their high CO_2 permeability, good thermochemical stability, low fabrication cost, and fast production process. In this research, a novel ternary MMM was fabricated via the blending of poly (amide 12-*b*-ethylene oxide) (PEBAX-1074) with polyethylene glycol (PEG-200) and magnesium oxide (MgO) nanoparticles mixture. The effects of various loadings of the fillers on CO_2, N_2, and CH_4 permeability values through the membranes were studied. Permeation of CO_2, N_2, and CH_4 gases through the resultant membranes at pressures of 2, 4, 6, 8, and 10 bar and temperatures of 25, 35, 45, and 55 °C revealed the superiority of the MMMs for CO_2/CH_4 and CO_2/N_2 separation in comparison with the pristine membranes. Particularly, at 25 °C and 2 bar, the CO_2 permeability, as well as ideal CO_2/CH_4 and CO_2/N_2 selectivity of the optimized MMM containing 40 wt% of PEG-200 and 8 wt% of MgO nanoparticles, rose to 210.1 Barrer, 24.9 and 60.9, corresponding to enhancement of around 225%, 23% and 24% of the CO_2 permeability and selectivity compared to the neat membrane, respectively. Thus, the fabricated MMM has a satisfying potential to separate CO_2 from N_2.

Keywords: MgO Nanoparticles, PEG-200, PEBAX-1074, Gas Separation Membrane

INTRODUCTION

Worldwide, burning of fossil fuels emits around 36 billion tons of carbon dioxide (CO_2), the largest source of greenhouse gases, annually [1]. The CO_2 emissions regulation justifies the design of advanced, economical technologies for CO_2 capture; consequently, the CO_2 recovery from enormous emission sources is a challenging effort that has absorbed significant consideration for many years [2]. Moreover, 20% of various natural gases formed all over the world per year need special treatment, as CO_2 may sometimes include up to 70% of the natural gas volume. The higher CO_2 concentration can cause the corrosion of a gas pipeline, as well as the reduction of the natural gas heating value. Old-style techniques of CO_2 capturing are absorption-based processes, like the well-known amine washing process, but these methods are highly energy-demanding and lead to environmental anxiety [3,4].

Lately, membrane-based technology for gas separation has been highly regarded due to its high performance, simplicity in scale-up and merging with other gas separation processes, low energy requirement, and low operational cost. Additionally, polymer-based membranes are preferred to other membrane materials because of their remarkable properties, such as low fabrication costs and high processability [5,6]. Copolymers have been used for many years as the primary materials for membrane preparation. Polyurethanes were the first copolymers which were used for membrane fabrication, and then this was followed by other materials, such as polyamides, polyimides, and various kinds of block copolymers [7]. As the block copolymers contain remarkable structural compatibility, they would be appropriate candidates as polymer-based membrane materials for improved gas transport [8]. One of the copolymers known as a desirable applicant for CO_2 separation from non-polar gases is polyether-block-amide with the commercial name "PEBAX" [9,10]. PEBAX is nearly a new class of beneficial elastomers with the overall structure of $(PA\text{-}PE)_n$. This polymer has linear chains of soft polyether (PE) and rigid polyamide (PA) sections, which are both relatively short blocks. The hard and soft parts are glassy and rubbery at ambient temperature, respectively. The ratio of PA to PE blocks in PEBAX defines the polymer's overall hardness, and the PA segment length generally influences its melting point [11,12]. As the PA and the PE sections are not miscible, PEBAX exhibits a bi-phase separation morphology [13,14]. It is a motivating candidate for CO_2 removal from natural, synthesis, and flue gases owing to its good polar/non-polar separation factor, such as CO_2/N_2 and CO_2/CH_4 selectivity coefficients. The PE block of the polymer functions as the permeable phase regarding the high mobility of its chains, while the PA part operates as the impermeable phase [15,16]. In the present work, PEBAX-1074 comprising 45 wt% of PA and 55 wt% of PE has been selected as the polymeric matrix for preparing MMMs [17,18].

The most straightforward technique to elevate gas transport per-

†To whom correspondence should be addressed.
E-mail: n_azizi@alumni.iust.ac.ir
Copyright by The Korean Institute of Chemical Engineers.

formance in polymeric membranes is physically mixing functional additives with the polymer mediums. Since the composite membranes' performance strictly depends on the characteristics of additives and polymers, the fillers or additives should be carefully chosen to blend with the primary polymers [19]. Recent investigations show that the incorporation of fillers into the polymers' mediums has nearly complex influence on the gas permeability value. Occasionally, the filler may be a polymer that can operate as a plasticizer and raise the free volume of the main polymer by separating the macromolecular chains. It can also reduce the intermolecular forces, as well as the energy of activation, leading to an increase in the polymer chains' mobility and corresponding rise in gas molecules transfer. Furthermore, the filler incorporation into the polymer matrix may change the polymer glass transition temperature due to the local segmental movements that, accordingly, alter the diffusion coefficients [20,21]. As there are ethylene oxide (EO) elements in polyethylene glycol (PEG), it would be a suitable plasticizer, which typically increases the permeability of CO_2, as well as CO_2/non-polar gases selectivity. Previous studies indicated that for a low molecular mass PEG, interactions among the macromolecule chains end groups and CO_2 molecules are greater, which can enhance the CO_2 solubility in the PEG [22,23]. Thus, PEG-200 was chosen as the plasticizer to blend with the PEBAX and fabricate blended membranes (BMs).

As the other additives, nanoparticles can be combined with polymers, improving the separation efficiency of resultant membranes. Besides, blending the inorganic phase and polymer matrix may develop the polymeric membranes' thermochemical stability. These membrane types are known as mixed-matrix membranes (MMMs) [24]. For the separation of CO_2 from CH_4 or N_2, the employed nanoparticles in the synthesis of MMMs should be chosen in such a way as to have an adequate CO_2 solubility capacity or let the CO_2 molecules transit the pores of the particles easily in case they are porous. In earlier studies, MgO nanoparticles held a high CO_2 adsorption capacity in comparison with CH_4 and N_2 [25,26]. MgO properties were combined with its low cost and make MgO nanoparticles a desirable additive for the PEBAX/PEG matrix.

So far, research has been accomplished on the fabrication of PEBAX-based MMMs for the separation of different gases [27,28]. However, only some studies have investigated the influence of PEG along with inorganic additives incorporation on the gas transport efficiency of PEBAX-based membranes. In a survey by Khosravi et al., the PEBAX-based MMMs were fabricated using polyethylene glycol-ran-polypropylene glycol (PEG-ran-PPG) and copper benzene-1, 3, 5-tricarboxylate (Cu_3BTC_2) fillers for studying CO_2 and CH_4 permeation characteristics of the membranes. The results showed that the CO_2 permeability and the ideal selectivity of CO_2/CH_4 were reached from 97.6 Barrer and 16.4 to 702.5 Barrer and 23.4, respectively, for the MMM loaded with 32.8 wt% of PEG-ran-PPG and 20 wt% of Cu_3BTC_2, compared with the neat PEBAX membrane [29]. Jazebizadeh et al. prepared PEBAX/PEG/ZnO MMMs to investigate their gas (CO_2 and CH_4) transport properties. Their results showed the CO_2 permeability and the ideal CO_2/CH_4 selectivity of the optimized MMM, composed of 4 wt% of ZnO nanoparticles and 40 wt% of PEG-400, compared to those of the pristine membrane, were reached from 44.6 Barrer and 20.4 to 94.5 Barrer and 24.0, respectively [30]. Wang et al. synthesized MMMs by incorporating PEG and multi-walled carbon nanotube (MWCNT) to study permeation characteristics of N_2, CH_4, and CO_2 through the prepared membranes. The outcome reveal that for the optimized MMM, including 40 wt% of PEG (PEGDME) and 5 wt% of MWCNT, the CO_2 permeability, the CO_2/CH_4 selectivity, and the CO_2/N_2 selectivity of 460 Barrer, 9.1, and 88.6 were acquired, respectively. The corresponding values for the neat membrane were 88.4 Barrer, 20.4, and 49.4 [31]. In another research, Mahmoudi et al. fabricated MMMs by adding PEG and nanozeolite X (NaX) into PEBAX. The effects of the additives on the permeability of CO_2 and CH_4 and the selectivity of CO_2/CH_4 in the membranes were investigated. The results revealed that the best efficiency was attained for the PEBAX membrane composed of 30 and 10 wt% of PEG and NaX, respectively. The CO_2 permeability and the CO_2/H_4 selectivity for the optimized membranes were 82.2 Barrer and 30.7, while those values were 65.9 Barrer and 21.5 for the pristine PEBAX membrane [32]. Chen et al. also prepared the PEBAX-based MMMs for CO_2/flue gas separation. The synthesized membranes had four different layers: PDMS, PEBAX/PEG, zeolite Y, and PES as the cover, selective, inorganic, and support layers, respectively. The permeation results of a mixed gas containing 20% of CO_2 and 80% of N_2 through the membrane of a single selective layer and the optimum MMM (the selective layer contains 25 wt% of PEBAX and 75 wt% of PEGDME-500 and shows a thickness of about 400 nm) exhibited the CO_2 permeance of 342 and 940 GPU and the CO_2/N_2 selectivity of 32 and 30, respectively [9].

A literature review revealed that it is the first attempt to investigate the influence of PEG-200 and MgO fillers addition into the PEBAX-1074 matrix. Thus, this work prepared novel ternary PEBAX/PEG/MgO MMMs and studied the gases (CO_2, N_2, and CH_4) transport properties of prepared PEBAX-based membranes. Furthermore, for better observation of the separation efficiency of the synthesized membranes, the influence of different parameters, such as PEG-200 and MgO concentrations, as well as operating conditions (feed temperature and pressure), on the CO_2 permeability and CO_2/CH_4 selectivity of the membranes was investigated. The resulting membranes were also characterized through FESEM, XRD, and FT-IR spectroscopy.

EXPERIMENTAL

1. Materials

In this work, the PEBAX-1074 (ρ=1.07 g cm^{-3}, T_g=−55 °C, and T_m=158 °C) in the pellet form, which was applied as a base polymer for the membrane preparation, made available by Arkema Co. PEG-200 (ρ=1.124 g cm^{-3}, and μ=60 MPa s) was purchased from Sigma-Aldrich Inc. MgO nanoparticles (ρ=3.58 g cm^{-3}, SSA=60 m^2 g^{-1}, and APS=20 nm) pack was obtained from US Research Nanomaterials, Inc. Dimethylformamide (DMF) which was employed as the solvent for the membrane preparation provided by Merck Co. CO_2, CH_4, and N_2 gases with purities of 99.995% were obtained from the Farafan Gas Tehran Company.

2. Membrane Preparation

In the current study, the membranes were prepared by solution casting-solvent evaporation. To fabricate films of the pristine mem-

brane, first, PEBAX-1074 pellets were placed for 12 h at 80 °C in a vacuum oven to make them moisture-free. After that, a mixture of the polymer and the DMF solvent with a concentration of 2.5 wt% was magnetically stirred at 100 °C for 3 h. Before the casting process, the solution was refined using a steel filter to obtain a homogeneous polymer solution. The filtered solution, which was then cast within Petri dishes, was placed in the oven at 50 °C. The membrane drying process lasted about 14 h. Then, n-hexane was employed to detach the fabricated membranes from the Petri dishes surfaces, and later to remove the residual solvents, they were put in a vacuum oven at 70 °C for 5 h [33,34]. Here, the prepared neat membrane was named NM.

Blended membranes were prepared by physical mixing of PEBAX-1074 and PEG-200 [35]. For this purpose, various PEG-200 amounts based on the PEBAX mass (10, 20, 30, 40, and 50 wt%) were blended with the DMF and stirred with a magnetic stirrer at room temperature for one hour. PEBAX granules were then poured into the fabricated solution and magnetically stirred at 100 °C for 3 h. Then, the homogeneous solution of PEBAX and PEG was cast within the Teflon Petri dishes, and the drying process of the BMs was followed like the neat membranes [22,36,37]. Based on the PEG contents of fabricated BMs, they were named BM10, BM20, BM30, BM40, and BM50.

The most critical issue in the synthesis of polymeric MMMs is the accumulation of the nanofillers in the continuous phase. Although MgO nanoparticles are very applicable to synthesizing various MMMs, they are substantially apt to agglomerate. Three significant parameters can influence the stability of nanoparticles in a solvent: (1) nanoparticles surface energy; (2) a dispersing medium where the nanoparticles should be distributed; and (3) a dispersant or dispersing agent, which can prevent the agglomeration of the nanoparticles in the dispersing medium. Here, to have the proper medium, we tried to choose the high-viscosity DMF solvent for preparing the PEBAX-based MMMs. It can postpone the sedimentation of the nanoparticles and nearly fix their positions in the polymeric matrix as it offers a fast gelation speed to the polymeric solution. However, since the MgO nanoparticles have a higher density compared to the solution, they still tended to be precipitated in the PEBAX matrix and led to fundamental agglomeration problems in the synthesis process of the MMMs. Therefore, a powerful sonication process was followed as another strategy to reduce the surface energy of the MgO nanoparticles and disperse the nanoparticles in DMF. However, the results confirmed that the probe sonication was not suitable enough for the long-term stability of the prepared DMF-based suspension. To overcome this problem, physical surface modification of the nanoparticles was recommended to balance the nanoparticles and the solvent densities. Employing PEG as a commonly used surface-modifier for various particles has been reported in several researches [38,39]. As the PEG-200 was used for preparing the blended and MMMs in the current study, we decided to apply it as the surface-modifier of the nanoparticles. For this goal, the following procedure was pursued.

At first, specific quantities of the MgO nanoparticles were dispersed in deionized (DI) water via an ultrasonic bath for 30 min. Second, a particular amount of PEG-200 was poured into the mixture, where the nanoparticles were dispersed. Then it was strongly mixed at room temperature for 36 h to coat the nanoparticles with PEG thoroughly. At last, the surface-modified particles were obtained via vaporization of the DI water from the mixture, being poured into a rotary evaporator. The results showed that the surface-modified MgO nanoparticles suspension was stable for nearly 12 h, which was sufficient to make them dispersed when they were added into the PEBAX solution during the MMMs preparation process [36,40].

For MMMs synthesis, PEG with a concentration of 40 wt% based on the PEBAX mass was poured into DMF solvent, and the prepared mixture was stirred for one hour under normal operating conditions. After that, a certain amount of the nanoparticles (surface-modified MgO with 2, 4, 6, 8, and 10 wt% based on the polymer mass) were added to the mixture, blended by means of a magnetic mixer for one hour, and then a probe-type ultrasonicator was employed for 30 min to disperse the particles into the mixture. To enhance the interaction among the modified MgO nanoparticles and PEBAX, resulting in a better distribution of the particles in the polymeric solution, the specified amount of the PEBAX granules was gently (in three steps) added to the suspension of nanoparticles/solvent at the temperature of 100 °C. As the next step, the prepared mixture was again sonicated in an ultrasonic bath at 80 °C for 5 min to attain a desirable dispersal of the nanofillers in the PEBAX matrix. Subsequently, a desiccator that accommodated the prepared solution vessel, was linked to a vacuum pump to remove any formed bubble in the solution, and then it was cast within Teflon Petri dishes. The ternary membranes were dried as

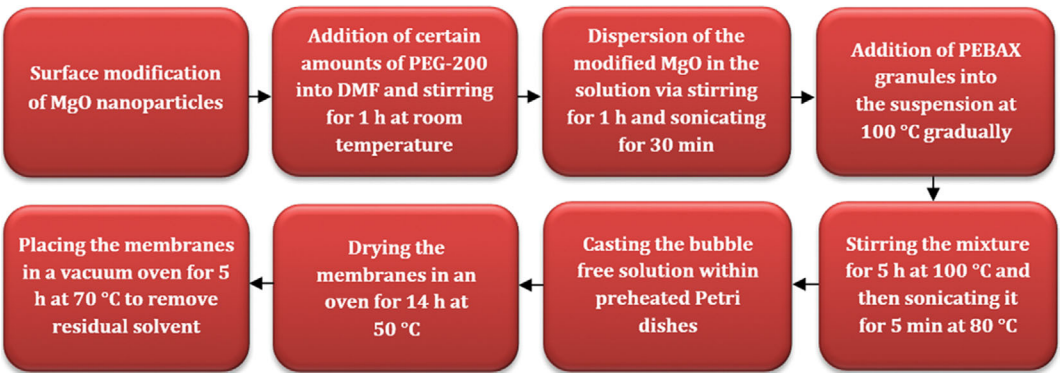


Fig. 1. Preparation mechanism of PEBAX-1074/PEG-200/MgO MMMs.

same as the pristine ones. After the final drying process, the prepared MMMs were brought out of the oven and retained in a desiccator until utilization. The thickness of the prepared membranes, being ascertained with a digital micrometer, was between 40 and 50 μm. The prepared ternary mixed-matrix membranes based on their nanoparticle contents were named TM2, TM4, TM6, TM8, and TM10. The preparation methodology of the MMMs is depicted in Fig. 1 [41,42].

3. Characterization

A JEOL X-ray diffractometer, model JDX-8030, was used to record X-ray diffraction. The device was equipped using a source of copper Kα, and the produced X-ray wavelength was nearly 1.541 Å. For identification of crystalline structure and inter-molecular distances among intersegmental chains of the resultant membranes, the angle of diffraction (2θ) was changed from 5° to 75°.

FT-IR spectra were obtained with a Shimadzu 8400S spectrometer, which was furnished via attenuated total reflectance (ATR). The spectra were in the range of 400-4,000 cm^{-1} under normal operating conditions, with 2 cm^{-1} spectral resolution.

Cross-sectional FESEM images of the prepared membranes were obtained applying a Sigma, Zeiss microscope. In addition to the morphology of the synthesized membranes, the quality of the surfaced-modified MgO nanoparticles distribution in the PEBAX matrix was investigated with the FESEM photographs. The membrane films were first cracked in liquid N_2, then coated with Au, and finally scanned with the electron microscope.

4. Gas Permeation Test

Permeation characteristics of N_2, CO_2, and CH_4 gases through the resultant membranes (flat-sheet films) were assessed at various temperatures of 25, 35, 45, and 55 °C and pressures of 2, 4, 6, 8, and 10 bar via a variable pressure (constant volume) setup, which is demonstrated in Fig. 2 [43-45]. A circular membrane with a 21.24 cm^2 effective area was placed inside a stainless-steel module and grasped tightly with two silicone O-rings. To measure gas permeation at different feed temperatures, the cell was located inside a temperature-controlled oven. Both membrane sides were evacuated for some hours, and then a leak experiment was performed. For starting the measurements, a specified gas was fed on a membrane side, whereas the permeate side was associated with a pressure transmitter recording the permeate side pressure as a function of time until the pressure change rate became constant. Subsequently, the curve slope $\left(\frac{dp}{dt}\right)_{s.s.}$ was employed to calculate the permeability in Barrer (1 Barrer=10^{-10} cm^3 (STP) cm cm^{-2} s^{-1} $cmHg^{-1}$) applying the following equation [5,44,45]:

$$P_i = \frac{22{,}414}{RT} \times \frac{V}{A} \times \frac{l}{\Delta p} \times \left(\frac{dp}{dt}\right)_{s.s.} \quad (1)$$

where A, V, R, T, l, Δp, and $\left(\frac{dp}{dt}\right)_{s.s.}$ are the surface area of a membrane sample in cm^2, the permeate side constant volume of the module in cm^3, the universal gas constant which is 6,236.56 cm^3 cmHg mol^{-1} K^{-1}, the absolute feed temperature in K, the thickness of the membrane in cm, the difference among the feed and permeate sides pressures in psi, and the pressure increase rate of the permeate side in cmHg s^{-1}, respectively. The ideal i/j selectivity (α_{ij}) was then calculated using:

$$\alpha_{ij} = \frac{P_i}{P_j} \quad (2)$$

where P_i and P_j are gases i and j permeability coefficients, respectively. To minimize the experimental errors, each experiment was carried out for three samples of each membrane, and the average results with the standard deviation were reported.

RESULTS AND DISCUSSION

1. Characterization

As mentioned, BMs containing various amounts of PEG-200 were synthesized in the current study. However, since the resulting membrane composed of 40 wt% of the PEG possessed the highest gas transport properties among the other prepared BMs, it was chosen for characterization.

One substantial evidence that can be used to examine polymeric membrane permeability is the investigation of their crystalline struc-

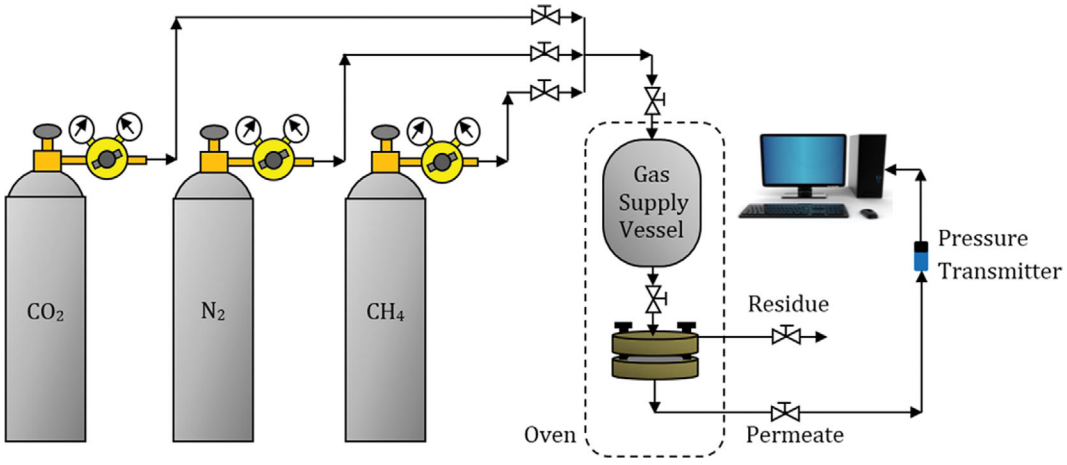


Fig. 2. Schematic of the constant-volume permeation setup.

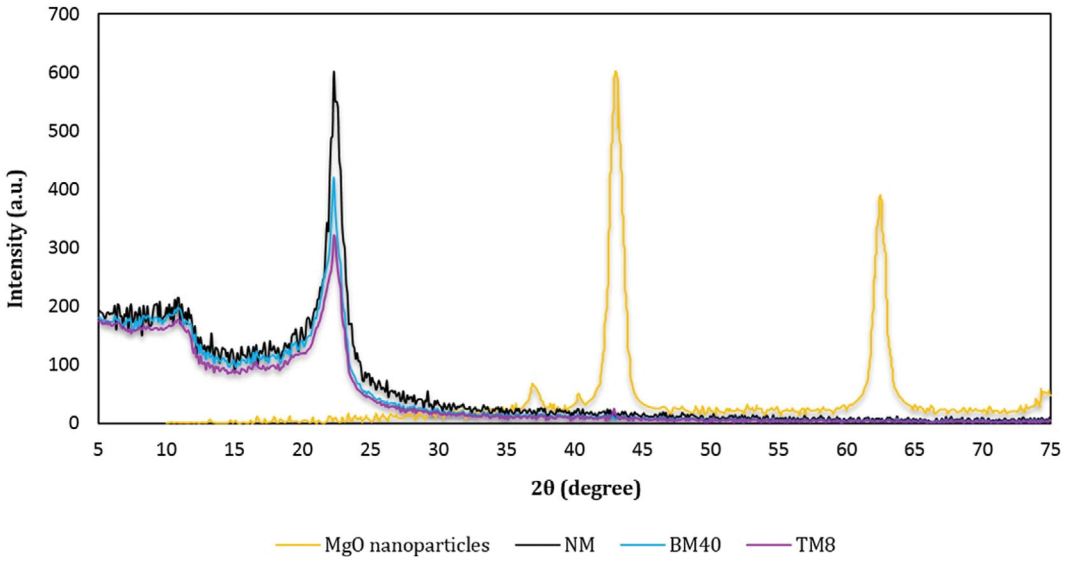


Fig. 3. XRD patterns of the MgO nanoparticles, NM, BM40 and TM8.

ture via XRD analysis [46,47]. XRD patterns of MgO nanofillers, the neat membrane (NM), the blended membrane loaded with 40 wt% of PEG (BM40), and the MMM incorporated with 8 and 40 wt% of MgO nanoparticles and PEG, respectively (TM8), are shown in Fig. 3. The XRD pattern of the semi-crystalline PEBAX-based NM exhibits a weak diffraction peak near 11°, which corresponds to the amorphous area, along with an intense one around 22° being attributed to the PEBAX crystalline region. Additive incorporation with a polymer matrix may change the crystalline characteristics and morphology of the main polymer. BM40 XRD patterns display that by the PEG-200 addition into the PEBAX matrix, the peaks' strengths at the crystalline and amorphous areas diminish. Hence, it can be inferred that the total crystallinity degree becomes smaller by combining the macromolecule into the main polymer matrix. The principal reason for this occurrence can be related to the hydrogen bonding rupture among the PA blocks in the BMs and, accordingly, the lessening of segments' cohesive energies [41, 42]. Additionally, Fig. 3 shows that the corresponding peak strength of the crystalline area declines by embedding the MgO nanoparticles within the polymer matrix. This decrease can also be ascribed to the inter-chain hydrogen bonding break among the PA blocks. Moreover, the XRD pattern of the MgO nanoparticles shows a sharp peak at around 43°, which can also be seen in the XRD pattern of the TM8. Since this peak is not intensive in the diffraction pattern of the TM8, it can be concluded that the MgO nanoparticles were distributed well in the membrane's polymeric matrix.

The position of the crystalline diffraction peak of a polymeric membrane beside its crystallinity is important for studying the membrane's permeation features. Based on Bragg's equation ($n\lambda=2d\sin\theta$), the decrease in 2θ values enhances the d-spacing (d) values. D-spacing can be defined as the molecular distance among the polymer chains. The greater the d-spacing value, the more potential for gas molecules passage [48,49]. As presented in Fig. 3, for NM, BM40, and TM8, the crystalline diffraction peaks are at 2θ=22.4°, 22.1°, and 21.9°, and the corresponding d-spacing values for the membranes are 3.96, 4.02, and 4.06 Å, respectively. Increasing the d-spacing value leads to an increase in the polymer volume (V) and, subsequently, a rise in fractional free volume (FFV) according to its definition ($FFV=1-\frac{V_0}{V}$). Therefore, the FFV of the polymeric matrix of the investigated membranes follows this order: TM8>BM40>NM. Enhancing the FFV means more free area among the polymer chains, which can cause a higher diffusivity and permeability of gas molecules through the membrane. As can be seen in the Cohen-Turnbull model ($D=A\exp(-\frac{\gamma v^*}{FFV})$), the diffusion coefficient (D) increases by the growth of FFV of the membranes [12,50].

Expectedly, by augmenting PEG-200 in the PEBAX matrix and MgO nanoparticles in the PEBAX/PEG matrix, improvements in gas permeability are observed due to the increment in FFV of the polymeric matrix and the decrement in the crystallinity of the membranes. This expectation perfectly matches the gas permeation tests [42,51].

The effect of adding MgO and PEG-200 fillers on the chemical bond alterations of the PEBAX matrix was examined by comparing FT-IR spectra of MgO nanofillers, PEG-200, the NM, the BM40, and the TM8, as displayed in Fig. 4. The NM IR spectrum showed that the detected peak at 1,112 cm^{-1} corresponds to the ether group (-C-O-C-) symmetric vibration in the soft PEO part [52,53]. Two other peaks at 1,626 and 1,636 cm^{-1} showed the presence of the bonded and free -C=O groups in H-N-C=O, respectively. Moreover, the O-C=O group presence was corroborated by a peak at 1,734 cm^{-1} in the PA segment. Additionally, two peaks at 1,548 and 1,564 cm^{-1} were ascribed to the bonded and free bending vibrations of the -N-H group and those at 3,290 and 3,328 cm^{-1} to its hydrogen-bonded and non-hydrogen bonded stretching vibration in the PA segment, respectively [54,55]. Furthermore, the aliphatic -C-H bond stretching and bending vibration are recognized via two peaks at 1,460 and 2,922 cm^{-1}, respectively [56]. As can be

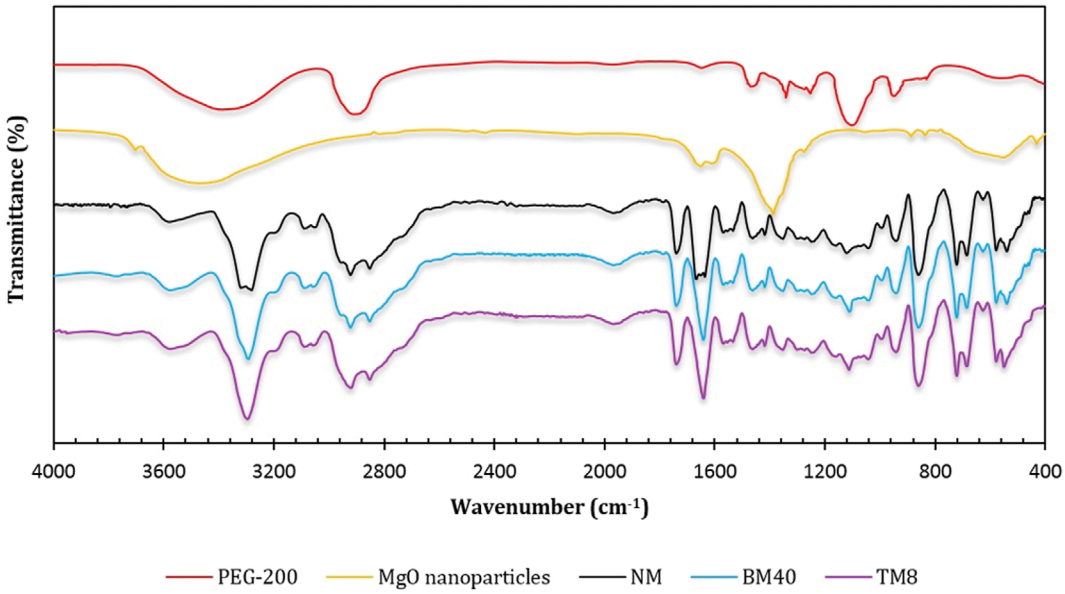


Fig. 4. FT-IR spectra of the PEG-200, MgO nanoparticles, NM, BM40 and TM8.

observed in Fig. 4, the PEG-200 IR spectrum displays three characteristic peaks, ascribed to -C-O-C-, -C-H, and -OH groups vibrations at 1,110, 2,918, and 3,403 cm^{-1}, respectively. Comparing the BM40 and NM spectra indicates that for the BM40, the -C=O and -N-H related peaks in H-N-C=O were shifted to the higher frequencies (the newly conforming peaks are at 3,292 and 1,640 cm^{-1}). The mentioned changes in the BM40 IR spectrum indicate the hydrogen bonding disconnection among the PA blocks and consequently, the BMs' crystallinity degree decrement [41,42]. These changes can be justified based on Hooke's law, described as Eq. (3) [57].

$$\upsilon=(1/2\pi c)(k/\mu)^{1/2} \quad (3)$$

where υ, k, and μ are indicative of the wavenumber, the force constant, and the reduced atomic mass of the chemical bond, respectively.

Moreover, the peak at 1,112 cm^{-1} allocated to the polymer ether group is strengthened with the PEG-200 incorporation into the PEBAX matrix due to the EO unit presence in the PEG. The MgO nanofillers FT-IR spectrum is also depicted in Fig. 4. The spectrum reveals a distinctive peak at 549 cm^{-1}, which corresponds to the Mg-O bond absorption. Comparing the TM8 IR spectrum with those of the NM and the BM40 shows that most of the peaks related to their functional groups can also be detected in the IR spectrum of the TM8. However, some variations among their FT-IR spectra are perceived. As previously explained, the PA groups are linked via hydrogen bonding; accordingly, there are two connected peaks around 1,626-1,636 cm^{-1}, corresponding to the free and hydrogen-bonded carbonyls in the PA blocks. After the MgO nanoparticles and the PEBAX/PEG matrix are combined, it can be found that the linked peaks change to a sole peak. In fact, the hydrogen bonding dissociation among the PA segments, resulting from the MgO embedment within the polymeric matrix, can be inferred. Additionally, the TM8 IR spectrum reveals a remarkable alteration in the -N-H stretching area. It is observable that the two linked peaks around 3,290-3,328 cm^{-1} were converted to an isolated peak and also shifted to a greater wavelength number after the MgO introduction. The changes in the ternary MMM represent that the interchain hydrogen bonds amongst the PA segments were partially disturbed due to the embedded MgO nanoparticles. Besides, comparing the membranes' IR spectra, another alteration can be seen in the TM8 spectrum, which is the presence of a weak peak near the wavenumber of 550 m^{-1} that corresponds to the Mg-O bond in the TM8 spectrum. As the mentioned peak is not intensified in the TM8 spectrum, it can be deduced that the MgO nanofillers were well-dispersed within the PEBAX/PEG matrix without their remarkable aggregation. The membrane characterization reveals a satisfactory match between the FT-IR spectroscopy outcomes and the XRD analysis results [48,56].

To study the effect of PEG-200 and MgO addition on the morphology of the prepared membranes, cross-sectional FESEM photos of the NM, BM40, and ternary MMMs comprising various loadings of MgO nanoparticles (2, 4, 6, 8, and 10 wt%) were illustrated in Fig. 5. As displayed in Fig. 5, all the synthesized membranes are of dense structures, and at the captured magnifications there are no significant voids. The cross-sectional SEM images show that the NM body structure is more uniform than that of the BM40. Regarding the XRD results, PEG-200 blending with the PEBAX matrix reduced the polymer crystallinity via rupturing the hydrogen bonding of the PA segment, leading to the nearly non-regular structure of the resulting membrane. As a result, the blended membrane structure is more irregular than that of the NM, as displayed in Fig. 5(b) [41,58]. Important information based on the MgO distribution quality in the ternary MMMs, affecting their gas transport characteristics, can also be achieved from the FESEM images. The images of the resultant MMMs composed of various content of MgO nanofillers (0-8 wt%) are illustrative of the uniform dispersal of the MgO nanoparticles in the PEBAX/PEG matrix without note-

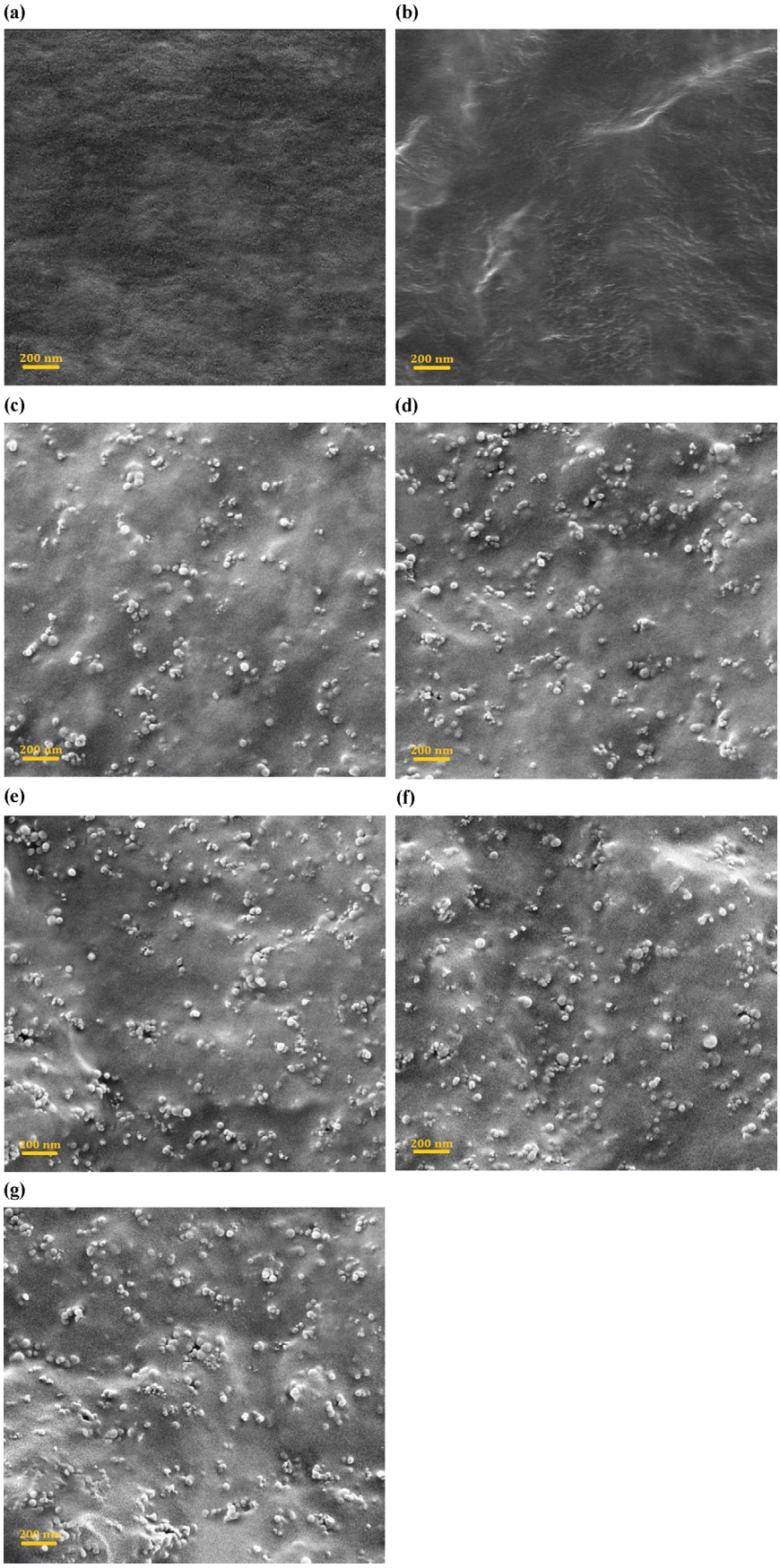


Fig. 5. Cross-sectional FESEM images of (a) NM, (b) BM40, (c) TM2, (d) TM4, (e) TM6, (f) TM8, and (g) TM10.

worthy defects or voids at PEBAX-MgO interfaces. However, some voids in angstroms can be observed around the particles if the FESEM images are highly magnified. Incompatibility between the surface of the MgO nanofillers and the polymeric matrix forms voids at the polymer-nanoparticles interface [40]. The FESEM images also indicate the clear nanoscale scatter of the MgO particles. The membrane's polymeric phase, whose color is gray, is representative of the PEBAX matrix. In contrast, its inorganic phase, which corresponds to the MgO nanoparticles, is in the form of white spheres. Utilization of some external forces (i.e., strong sonication) is able to make the modified MgO particles well-distributed in the solvent and, accordingly, in the polymeric matrix. Insufficient attractive force among the surface-modified nanofillers avoids their accumulation and permits the MgO particles to spread uniformly in the membranes' polymeric matrices. Actually, the PEBAX/PEG mixture and the surface-modified MgO nanoparticles can interact together with dipole-dipole and van der Waals interactions that may lead to a stable MgO particles suspension in the DMF and, therefore, their fine distribution in the polymeric matrix. As shown in Fig. 5, surface-modified MgO nanofiller distribution in the PEBAX/PEG matrix was uniform at lower content (such as 2, 4, and 6 wt%), whereas their accumulation was substantial at higher loading (8 and 10 wt%) [59,60]. High attractive energy among the MgO nanoparticles, a considerable difference between the nanoparticles and the polymer solution surface energies, as well as the higher density of MgO nanoparticles than the polymeric solution are the main reasons for the agglomeration and sedimentation of the nanoparticles in the polymer matrix at the high loading of MgO nanoparticles.

2. Gas Permeation Characteristics

2-1. Influence of PEG-200 Loading

For the PEBAX-based membranes, the permeability of CO_2 in the polymeric matrix is higher than that of CH_4 and N_2 as CO_2 has a higher critical temperature (T_c of CO_2 is 31.1 °C, while that of CH_4 and N_2 is −82.3 °C and −146.9 °C, respectively), and a lower kinetic diameter (kinetic diameter of CO_2 is 3.3 Å, whereas that of N_2 and CH_4 is 3.64 and 3.8 Å, respectively). Besides, the PEBAX polar group affinity to CO_2 is more than non-polar gases (N_2 and CH_4). Actually, the lower solubility of non-polar gases in the polymer matrix, as well as their smaller diffusivity because of their larger kinetic diameters, brings about lower permeabiliy compared to that of CO_2 [48].

Gas permeation through the BMs was surveyed to evaluate the added PEG-200 effect on the resulting membrane transport features. For this examination, the temperature and pressure of the feed were fixed at 25 °C and 2 bar, respectively, for all the prepared membranes. As observed in Fig. 6, the PEG-200 content increment in the PEBAX matrix from 0 to 50 wt% led to a significant increase of CO_2 permeability from 64.63 to 165.19 Barrer, whereas the permeability of CH_4 and N_2 gases did not change remarkably (permeability of these gases was enhanced from 3.19 and 1.31 to 7.98 and 3.25, respectively). Notably, the gas permeability of dense polymer-based membranes follows the solution-diffusion procedure; therefore, alterations in both gases' solubility and diffusivity need to be surveyed to determine the PEG content effect on permeability. Penetrant diffusivity would be enhanced by the addition of PEG-200 with regards to the FFV increment; the PEG can play a role as a plasticizer and embed its molecules among the polymer chains, creating additional inter-molecular space for Brownian movement and, accordingly, flexibility increase of the polymer chains [61]. Previously, the XRD analysis showed that the PEG-200 blending with the PEBAX-1074 matrix reduced the crystallinity of the BMs due to the disruption of the PA inter-molecular hydrogen bonding. Consequently, the gases tended to diffuse more into the resultant membranes [31,41]. Moreover, more permeability of CO_2 compared to CH_4 and N_2 through the BMs is expected due

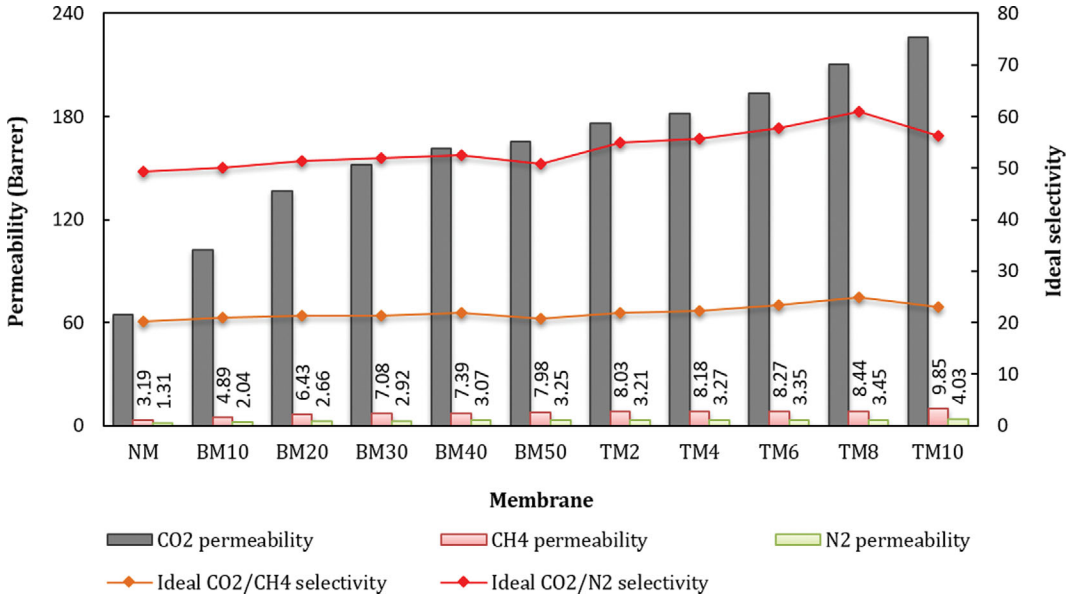


Fig. 6. Influence of PEG-200 and MgO nanoparticles loading on gas permeation property of the prepared PEBAX-based membranes at 2 bar and 25 °C.

to the existence of the EO units of PEG in the membrane matrices, which can increase CO_2 solubility due to its good affinity for the ether groups. Consequently, the CO_2 solubility, as well as its permeability, increases more than that of N_2 and CH_4 by enhancing the PEG content; therefore, the ideal CO_2/N_2 and CO_2/CH_4 selectivity increases from 49.33 and 20.26 to 52.56 and 21.84, respectively, as the PEG-200 loading increases from 0 to 40 wt%, as illustrated in Fig. 6 [22,37]. However, with further enhancing the PEG content from 40 to 50 wt%, the ideal CO_2/CH_4 and CO_2/N_2 selectivity experiences decreasing trends. As an example, for the BM50, the CO_2/CH_4 selectivity and that of CO_2/N_2 were 20.70 and 50.82 at 25 °C and 2 bar. These reductions can be due to the great increment of CH_4 and N_2 resulting from micro-phase separation. With raising the PEG loading more than 40 wt%, the distributed PEG molecules find a chance to get close to each other, forming PEG-rich phases on a molecular scale in the Pebax/PEG matrix. As a result, CH_4 and N_2 molecules can diffuse more in the PEG liquid phase of the membrane and, accordingly, reduce the CO_2/CH_4 and CO_2/N_2 selectivity [62].

The results show that the prepared BMs loaded with 10, 20, 30, and 40 wt% of PEG-200 (BM10, BM20, BM30, and BM40) perform better for CO_2/CH_4 and CO_2/N_2 separation than the NM and, among the others, the BM40 has higher separation efficiency.

2-2. Influence of MgO Nanofillers Loading

As discussed earlier, because the BM40 provides higher separation proficiency than do the other prepared blended and neat membranes, the surface-modified MgO particles were embedded into the BM40 matrix with various loadings to reach the best efficiency. Fig. 6 depicts the effect of MgO nanofillers loading on gas permeation of resulting MMMs at constant pressure and temperature of 2 bar and 25 °C, respectively. The results show that the permeability of N_2, CH_4, and CO_2 gases increased when the MgO loading was increased. One possible reason for this phenomenon can be due to the formation of voids at the interfaces of the MgO nanoparticles and the PEBAX owing to the MgO nanoparticles and the PEBAX matrix inconsistency. The creation of these interfacial defects lets the penetrants diffuse more through the prepared membranes and also increases the FFV of the polymeric matrix. Furthermore, the diminished crystallinity of the MMMs due to the dissociation of inter-chain hydrogen bonding among the PA segment and, therefore, their improved FFV will be another reason for the greater MMMs gas permeability values compared to those of the NM and BMs [36,40].

Several researches have studied MgO particles' capacity for various gases' adsorption. The results revealed higher CO_2 adsorption on MgO nanoparticles compared to CH_4 and N_2 at a fixed temperature and pressure [63]. As observed in Fig. 6, CO_2 molecules, due to their increased solubility in the MMMs, resulting from the amazing capacity of the MgO nanoparticles for CO_2 adsorption, display a more remarkable rise from 161.37 at 0 wt% to 226.39 Barrer at 10 wt% content. Therefore, this higher CO_2 affinity to the nanofillers compared to the other gases' affinity can be the main reason for the higher CO_2/CH_4 and CO_2/N_2 selectivity of the prepared MMMs embedded with the MgO nanoparticles in comparison to the NM selectivity values. Thus, the ideal CO_2/CH_4 and CO_2/N_2 selectivity is enhanced from 21.84 and 52.56 to 24.89 and 60.90, respectively, with raising the MgO nanoparticles loading from 0 to 8 wt%, as observed in Fig. 6. The selective void formation at the polymer-nanoparticle interface so that only the CO_2 molecules can diffuse may be the other reason for the selectivity value improvement [64,65]. However, the results of the experiments reveal that by raising the MgO nanofillers from 8 to 10 wt%, ideal CO_2/CH_4 and CO_2/N_2 selectivity declines from their corresponding values to 22.98 and 54.82, respectively. The principal reason for this behavior is the creation of the non-selective voids at the polymer-nanoparticle interface because of the agglomeration of the MgO nanofillers in the polymeric matrix, which can cause more CH_4 and N_2 diffusion and transport through the membranes and consequent reduction in the selectivity. As a result, TM8 has the best selectivity for CO_2/CH_4 and CO_2/N_2 separation among all the prepared membranes.

2-3. Influence of Feed Pressure

To investigate the feed pressure influence on the permeation features of the fabricated membranes, permeability trends of pure N_2, CH_4, and CO_2 gases through the prepared pristine, blended, and ternary mixed-matrix membranes at a temperature of 25 °C and pressure limits of 2-10 bar are graphically depicted in Figs. 7(a) and 7(b). As shown in Fig. 7, the three gases' permeability values for all the resultant membranes improved with pressure rise. This behavior can be attributed to the increase of the mass transfer driving force, as well as the gas concentration in the polymer matrix, which could overcome the adverse effect of the pressure increase, which is the chain compactness of the polymeric membrane. For the dense polymeric membranes, solution-diffusion is the dominant mechanism for the permeation of a penetrant. In this mechanism, gas permeability is determined by the product of the penetrant gas solubility and diffusion coefficients ($P_i=S_i\times D_i$). As a result, the increase of the gas permeability with the pressure enhancement can be justified by the growth of the gas solubility coefficient [59]. Raising the feed pressure from 2 to 10 bar enhances the permeability of CO_2 through the NM from 64.63 to 90.85 Barrer, while it changes that of CH_4 and N_2 from 3.19 and 1.31 Barrer to 3.79 and 1.74 Barrer, respectively. As clearly observed, the permeability of CO_2 rises with a greater slope due to its higher solubility, which can be ascribed to its higher condensability, as well as superior affinity to the PEBAX polar ether groups. Also, the CO_2 kinetic diameter is less than that of CH_4 and N_2; consequently, CO_2 molecules can penetrate further than N_2 and CH_4 when the feed pressure increases. Hence, the ideal CO_2/CH_4 and CO_2/N_2 selectivity of the NM increases from 20.26 and 49.34 to 23.97 and 52.21, respectively, with increasing feed pressure, as in Fig. 7(c). This behavior can also result from the plasticization effect of condensable acid gases like CO_2 in the PEBAX matrix due to the pressure increment [59].

As shown in Figs. 7(a), 7(b), and 7(c), the gas permeability through the prepared BMs increases more than that through the NM. For example, CO_2, CH_4, and N_2 permeability through the BM40 increases from 161.37, 7.39, and 3.07 Barrer to 212.28, 8.08, and 3.82 Barrer, respectively. This can be because as the pressure is enhanced, the gases can diffuse easier through the blended membranes than the neat membrane because of the liquid PEG in the polymeric matrix of the BMs. Thus, penetrant diffusivity in a liquid can be improved more than that in a solid by increasing the feed pressure.

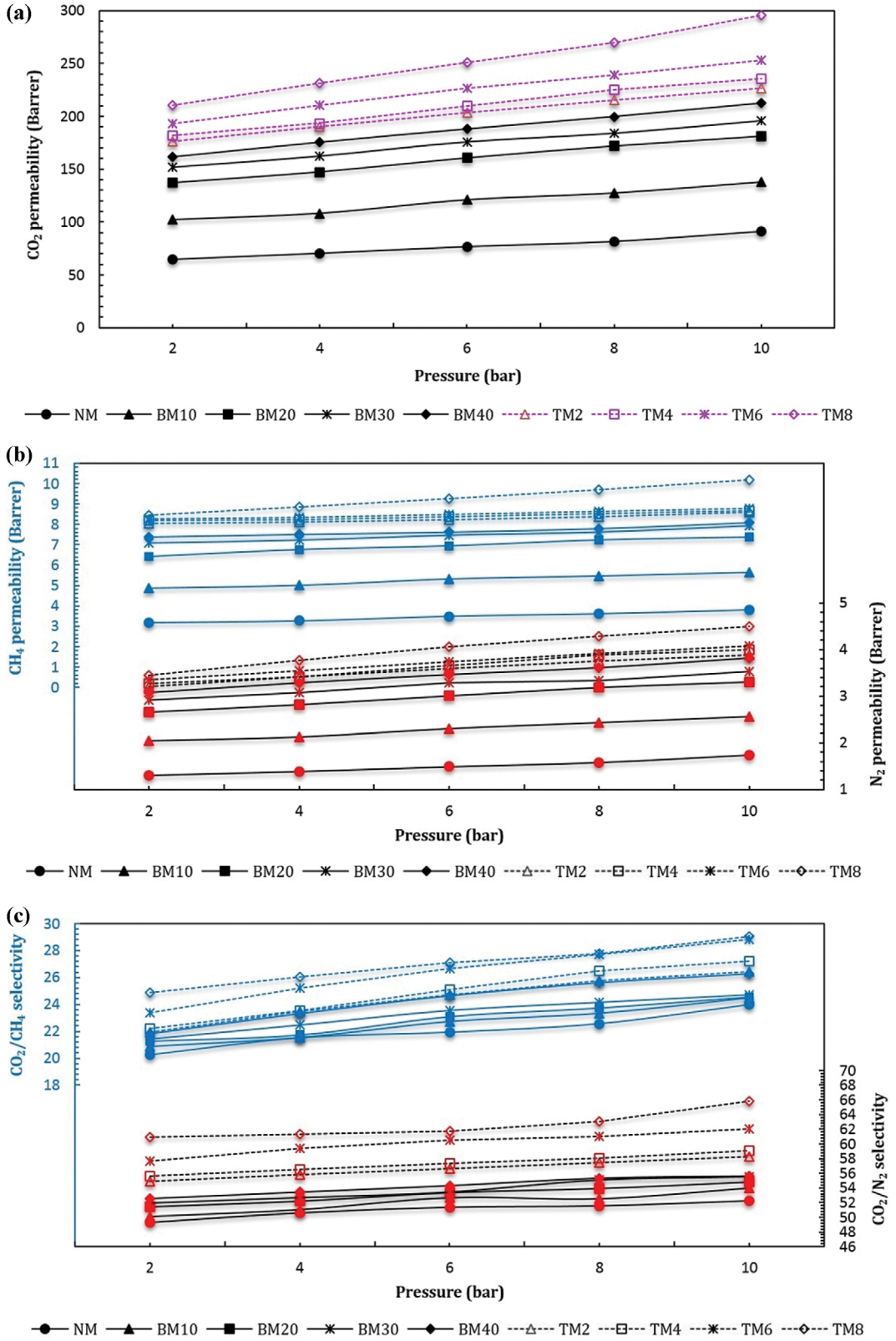


Fig. 7. Effect of feed pressure on permeabilities of (a) CO_2, (b) CH_4 and N_2 and (c) ideal CO_2/CH_4 and CO_2/N_2 selectivity of the prepared membranes at 25 °C.

However, with increasing pressure, the permeability increment of CO_2 through the BMs is relatively greater than that for CH_4 and N_2 owing to CO_2 more solubility in the BMs, resulting from the added EO units with high CO_2 affinity into the BMs' matrices. As

a result, the ideal CO_2/CH_4 and CO_2/N_2 selectivity of the blended membrane reaches from 21.84 and 52.56 to 26.27 and 55.57, respectively [22,40].

As also seen in the figures, compared to the gas permeability

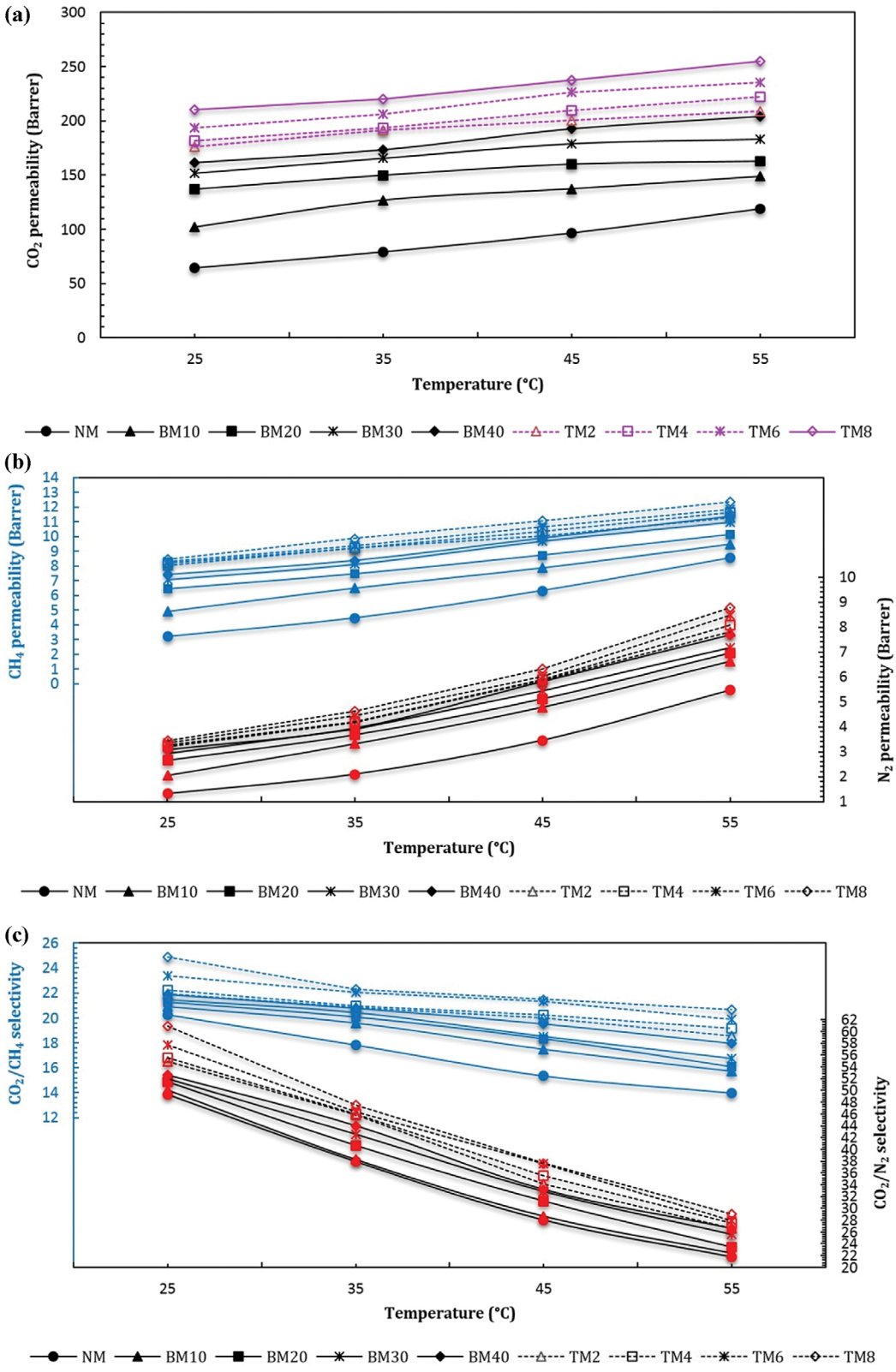


Fig. 8. Effect of feed temperature on permeabilities of (a) CO_2, (b) CH_4 and N_2 and (c) ideal CO_2/CH_4 and CO_2/N_2 selectivity of the prepared membranes at 2 bar.

through the pristine and blended membranes, the gas permeability, particularly CO_2 permeability through the prepared MMMs, increases more. For instance, for the TM8, with growing pressure from 2 to 10 bar, the CO_2 permeability rises from 210.12 to 295.44 Barrer, whereas CH_4 and N_2 permeability increases from 8.44 and 3.45 Barrer to 10.18 and 4.49 Barrer, respectively. The increase of the MMMs' capacity for gas adsorption due to the enhanced adsorption capacity of the incorporated MgO nanoparticles with pressure is the main reason for the superior increment of gas permeability through the MMMs in comparison to the NM and BMs. However, with the pressure increase, the CO_2 adsorption capability of the MgO particles is intensified more than their ability for CH_4 and N_2 adsorption; as a result, this behavior enables CO_2 to permeate more through the MMMs, resulting in their higher ideal CO_2/CH_4 and CO_2/N_2 selectivity. As a consequence, the ideal CO_2/CH_4 and CO_2/N_2 selectivity of the TM8 rises from 24.89 and 60.90 to 29.02 and 65.80, respectively [62,66,67].

2-4. Influence of Feed Temperature

Figs. 8(a), 8(b), and 8(c) exhibit the influence of the operating temperature on the CO_2, CH_4, and N_2 gas permeabiliy and ideal CO_2/CH_4 and CO_2/N_2 selectivity of the fabricated neat, blended and mixed-matrix membranes at the constant pressure of 2 bar. Increasing the temperature from 25 to 55 °C increases the gas permeability through all the membranes. For example, the CO_2 permeability of the NM increases from 64.63 to 119.05, while its CH_4 and N_2 permeabilities alter from 3.19 and 1.31 to 4.89 and 2.04, respectively. The enhanced gas permeability can be due to increased polymer chains' movement by the temperature rise [68]. As observed, the permeability of N_2 and CH_4 rises more than that of CO_2 with a temperature rise. This can also be explained by looking at Arrhenius types of the equation describing temperature dependency of transport properties through dense polymeric membranes, as follows:

$$D_i = D_0 \exp\left(\frac{-E_d}{RT}\right) \tag{4}$$

$$S_i = S_0 \exp\left(\frac{-\Delta H_s}{RT}\right) \tag{5}$$

$$P_i = D_i \times S_i = P_0 \exp\left(\frac{-E_p}{RT}\right) \tag{6}$$

Where, E_d, ΔH_s, and E_p are the activation energy for diffusion, the solution heat ($\Delta H_s = \Delta H_{Condensation} + \Delta H_{Mixing}$), and the activation energy for permeation ($E_p = E_d + \Delta H_s$), respectively. $\Delta H_{Condensation}$ is the molar heat of condensation of the penetrant, and ΔH_{Mixing} is the partial molar heat of mixing. Since E_d is ordinary positive, the diffusivity (D_i) of all the gases will rise with the temperature increment [59, 68]. Besides, condensation is an exothermic process and, therefore, $\Delta H_{Condensation}$ is negative in any case. This is much more overcoming for condensable gases than ΔH_{Mixing}, which is mostly positive. Therefore, ΔH_s, which equals the sum of $\Delta H_{Condensation}$ and ΔH_{Mixing}, is expected to be negative for CO_2. However, for the non-interacting gases (CH_4 and N_2), being above their critical temperatures at the ambient conditions, dissimilar to the soluble gas (CO_2), $\Delta H_{Condensation}$ is ignorable and ΔH_{Mixing}, due to the weak interaction between CO_2 and the polymer, plays a crucial role. Kim et al. reported different terms of E_d, E_p, and ΔH_s for N_2, CO_2, O_2, and He in PEBAX [59]. Their study showed that ΔH_s of N_2, He, and O_2 was positive, whereas it was negative for CO_2. In brief, for some gases like CO_2, whose the ΔH_s is negative, the temperature increase leads to solubility decrement, while for non-condensable light gases such as N_2 and CH_4, the solubility rises. Hence, as the E_p of CH_4 and N_2 is higher than CO_2, the CH_4 and N_2 permeabilities grow more than that of CO_2 when the temperature is enhanced. Expectedly, the ideal CO_2/CH_4 and CO_2/N_2 selectivity values exhibit decreasing trends by a temperature increase (see Fig. 8(c)). Notably, the permeability of all gases increases with temperature, which signifies more temperature-dependency of diffusivity than solubility.

For BMs, the same trend is seen in the gas permeability of NM with temperature rise. Also, it is observed that the enhancement in the permeability of all gases through the blended membranes is higher than that of the pristine membrane. PEG loading, as well as the temperature increase results in the gases' diffusion and, consequently, their permeation, as explained earlier. For example, for the BM40, the permeability of CO_2, CH_4, and N_2 increases from 161.37, 7.39, and 3.07 to 204.15, 11.36, and 7.68, respectively, as the temperature rises from 25 to 55 °C. As a result, CO_2/CH_4 and CO_2/N_2 selectivity values change from 21.84 and 52.56 to 17.97 and 26.58, respectively.

For MMMs, similar behavior in the gas permeability was detected. Their permeability through the resulting MMMs rises more than through the NM and BMs. This trend is most likely a result of two chief reasons: (1) the incorporated MgO nanoparticles into the polymeric matrix increase the solubility of the gases in the prepared membranes as temperature rises. (2) the temperature rise augments the polymer chain mobility around the nanoparticles and causes their more activity for the gas penetration. Actually, the temperature enhancement makes the gas diffusivity increase. As demonstrated in Fig. 8(c), the ideal CO_2/CH_4 and CO_2/N_2 selectivity for the TM8 declined from 24.89 and 60.90 to 20.68 and 29.03, respectively, with raising the temperature, which exhibits that the influence of the feed temperature rise on the permeability of CH_4 and N_2 is more than that of CO_2.

2-5. Stability of Prepared PEBAX-based Membranes

To evaluate the performance stability of the prepared membranes, the gas permeability and ideal CO_2/CH_4 and CO_2/N_2 selectivity through the NM, the BM40, and the TM8 were measured within 12 h, as demonstrated in Figs. 9(a) and 9(b). As depicted in the figures, the membrane efficiency remained relatively stable during 12 h tests of gas permeation without substantial variations in gas permeability and membrane ideal selectivity. However, due to the effect of plasticization, a slight increase in CO_2 permeability, as well as a reduction in the ideal selectivity of the fabricated membranes, was perceived [9]. As can also be seen in the figures, the stability of the TM8 is higher than that of the NM and the BM40 due to the high resistance of the incorporated MgO nanoparticles. In fact, the incorporated MgO with the PEBAX matrix decreased the plasticization effect and improved the performance stability of the resultant ternary MMM.

2-6. Comparison of this Study Results with the Literature

One commonly used method to examine the gas separation efficiency of polymeric membranes is considering their perme-

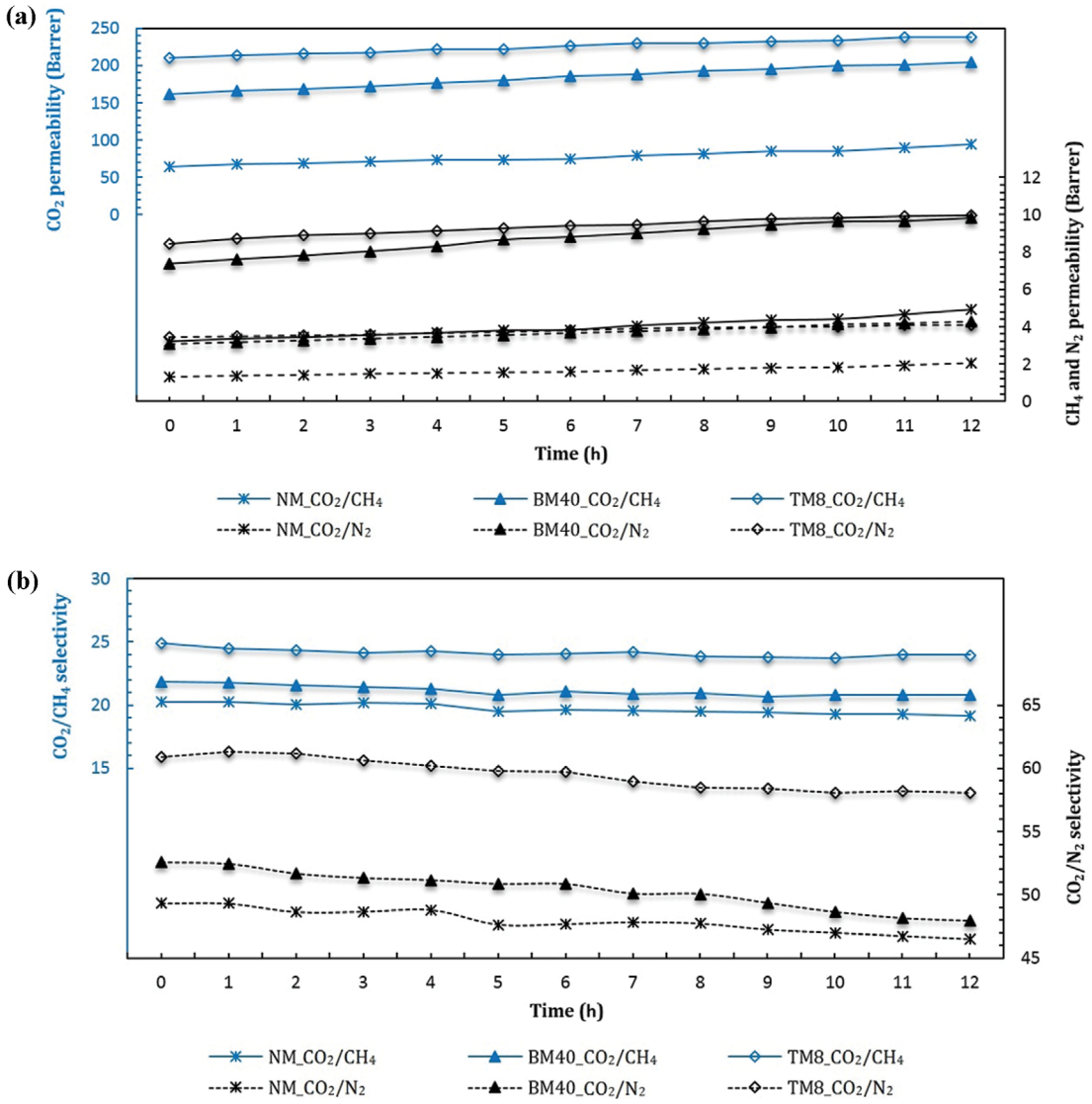


Fig. 9. (a) CO_2, CH_4 and N_2 permeability, (b) ideal CO_2/CH_4 and CO_2/N_2 selectivity of the NM, BM40 and TM8 versus time in 12 h stability tests at 2 bar and 25 °C.

ation data at a certain pressure and temperature in a permeability-selectivity plot, which is the so-called Robeson's chart. In such figures, for various gas pairs, Robeson offered experimental upper bound restrictions in 1991 and 2008 [69,70]. If the membrane data are placed above the proposed lines, it means that the preparation of that membrane is economically justified and, accordingly, it can be marketable. Hence, recently, researchers have tried to get to the region above the mentioned lines. As depicted in Figs. 10(a) and 10(b), the resulting MMMs performance for CO_2 removal from N_2 and CH_4 at the temperature and pressure of 25 °C and 2 bar, respectively, js compared with Robeson's upper bound lines. The figures illustrate that their permeation data, indicative of their efficiency, get adjacent to Robeson's limits by raising the PEG-200 and MgO nanofiller content up to 40 and 8 wt%, respectively, in the PEBAX-1074 matrix. However, the membrane performance declines and gets far from the limits as the PEG and MgO loading rises more than 40 and 8 wt%, respectively.

To further evaluate the prepared membranes, the permeability-selectivity values of other PEBAX-based MMMs presented in the literature are reported in Table 1, and those of ternary MMMs, including PEBAX and PEG in their structures, are in Figs. 10(a) and 10(b) [71]. The obtained outcomes indicate that permeability-selectivity data of the prepared ternary PEBAX/PEG/MgO MMM consists of 8% wt. of MgO nanofillers and 40% wt. of PEG-200 (TM8) are nearly closer to the lines suggested by Robeson in comparison with those of the other MMMs. Thus, for CO_2/CH_4 and CO_2/N_2 separation, the optimum MMM composed of 8 wt% of MgO and 40 wt% of PEG-200 shows comparatively better efficiency compared to similar PEBAX-based MMMs.

CONCLUSION

Presented here is the preparation of PEBAX-1074 based MMMs using PEG-200 and MgO nanoparticles as fillers. To characterize

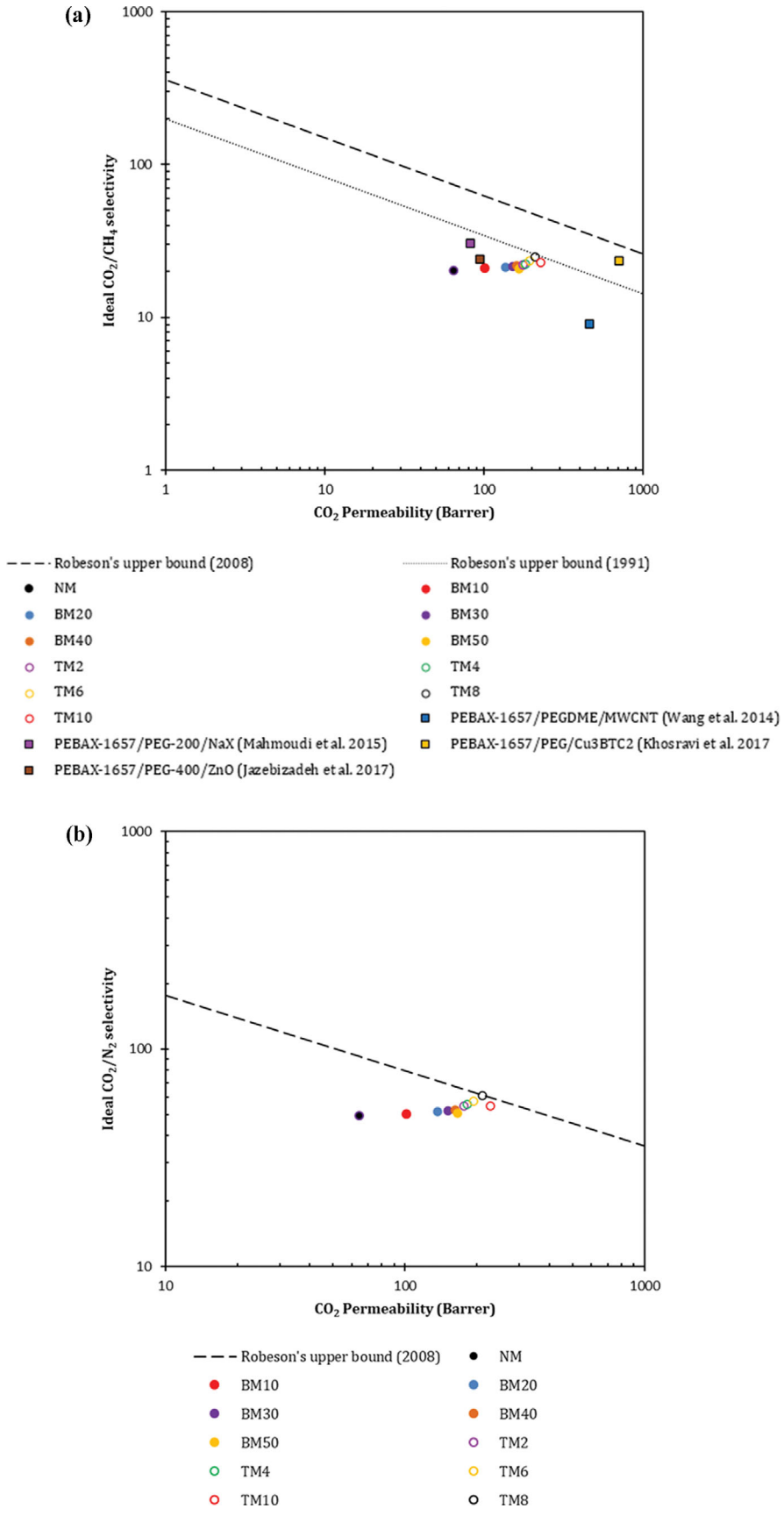


Fig. 10. Gas permeation efficiency of various PEBAX-based membranes for the separation of (a) CO_2/CH_4 and (b) CO_2/N_2 compared to the Robeson's upper bound limits.

Table 1. Comparison of the gas permeation performance of the optimized membrane in the current study with different PEBAX-based MMMs

Membrane type	Filler content (wt%)	Operating conditions	P_{CO_2} (Barrer)	α_{CO_2/CH_4}	α_{CO_2/N_2}	Ref.
PEBAX-1074/PEG-1500	30	5 bar 35 °C	25.7	10.6	34.6	Feng et al. 2013
PEBAX-2533/ZIF-8	35	2 bar 25 °C	1,287.0	9.0	32.3	Nafisi et al. 2014
PEBAX-1657/Zeolite 4A	5	5 bar 25 °C	71.4	32.2	52.8	Surya Murali et al. 2014
PEBAX-1074/SAPO-34	30	4 bar 25 °C	160.0	32.0	68.7	Rabiee et al. 2015
PEBAX-1657/NaX	2	3 bar 25 °C	32.3	---	98.0	Zarshenas et al. 2016
PEBAX-1657/Fumed silica	10	4 bar 25 °C	49.0	28.8	94.3	Aghaei et al. 2018
PEBAX-1657/FeBTC	30	3 bar 25 °C	329.7	20.5	---	Dorosti et al. 2018
PEBAX-1074/GTA	60	5 bar 25 °C	134.7	16.2	59.6	Feng et al. 2019
PEBAX-1074/ZIF-8	30	3 bar 25 °C	200.0	19.3	---	Atashjameh et al. 2020
PEBAX-2533/Sorbitol	15	2 bar 30 °C	320.7	12.4	46.5	Hassanzadeh et al. 2022
PEBAX-1657/PEA	3	2 bar 25 °C	195.8	23.3	---	Lv et al. 2022
PEBAX-1657/Cu	5	2 bar 25 °C	117.9	30.5	---	Hou et al. 2022
PEBAX-1657/PEGDME/MWCNT	PEGDME: 40 MWCNT: 2	2 bar 22 °C	460.0	9.1	88.6	Wang et al. 2014
PEBAX-1657/PEG-200/NaX	PEG: 30 NaX: 10	2 bar 25 °C	82.2	30.7	---	Mahmoudi et al. 2015
PEBAX-1657/PEG/Cu_3BTC_2	PEG: 32.8 Cu_3BTC_2: 20	3 bar 30 °C	702.5	23.4	---	Khosravi et al. 2017
PEBAX-1657/PEG-400/ZnO	PEG: 40 ZnO: 4	3 bar 25 °C	94.5	24.0	---	Jazebizadeh et al. 2017
PEBAX-1074/PEG-200/MgO (TM8)	PEG: 40 MgO: 8	2 bar 25 °C	210.1	24.9	60.9	This study

the prepared membranes, XRD, FT-IR, and FESEM analyses were conducted. The FT-IR and XRD results revealed that hydrogen bonds interlinking the PA segments were ruptured owing to the existence of the MgO and PEG-200 fillers. Moreover, as illustrated in the FESEM photos, adding the PEG-200 into the base polymer matrix, the resultant blended membrane indicates some structural irregularity compared to the pristine one. The cross-sectional images also show that the MgO nanoparticle distribution within the PEBAX/PEG matrix is nearly uniform, and the prepared PEBAX/PEG/MgO MMMs are almost defect-free. The gas permeation results exhibited that the MMMs show superior separation efficiency compared to the blended and pristine membranes under the same conditions due to the selective voids created at the polymer-MgO particles interface, their reduced crystallinity, their increased free volume, and their increased solubility resulting from the high CO_2 absorption capacity of the added MgO and PEG-200 fillers. Based on the CO_2 permeability, as well as ideal CO_2/CH_4 and CO_2/N_2 selectivity, it appears that the optimum performance of the MMMs is achieved at loadings of 8 and 40 wt% for MgO nanoparticles and PEG-200, respectively. The results also showed the MMM's high CO_2/N_2 separation ability.

DECLARATION OF COMPETING INTEREST

None.

REFERENCES

1. J. Guan, T. Huang, W. Liu, F. Feng, S. Japip, J. Li, X. Wang and S. Zhang, *Cell Rep. Phys. Sci.*, **3**, 100864 (2022).

2. A. Brunetti, F. Scura, G. Barbieri and E. Drioli, *J. Membr. Sci.*, **359**, 115 (2010).
3. D. D. Iarikov and S. T. Oyama, Review of CO_2/CH_4 separation membranes, Membrane Science and Technology, Elsevier, 914 (2011).
4. A. Husna, I. Hossain, I. Jeong and T.-H. Kim, *Polymers*, **14**, 655 (2022).
5. S. Meshkat, S. Kaliaguine and D. Rodrigue, *Sep. Purif. Technol.*, **200**, 177 (2018).
6. N. Azizi, M. Isanejad, T. Mohammadi and R. M. Behbahani, *Front. Chem. Sci. Eng.*, **13**, 517 (2019).
7. C. Park, J. Yoon and E. L. Thomas, *Polymer*, **44**, 6725 (2003).
8. A. Jonquières, R. Clément and P. Lochon, *Prog. Polym. Sci.*, **27**, 1803 (2002).
9. Y. Chen, B. Wang, L. Zhao, P. Dutta and W. W. Ho, *J. Membr. Sci.*, **495**, 415 (2015).
10. L. Zhao, Y. Chen, B. Wang, C. Sun, S. Chakraborty, K. Ramasubramanian, P. K. Dutta and W. W. Ho, *J. Membr. Sci.*, **498**, 1 (2016).
11. E. Konyukhova, A. Buzin and Y. K. Godovsky, *Thermochim. Acta*, **391**, 271 (2002).
12. N. Azizi, M. Arzani, H. R. Mahdavi and T. Mohammadi, *Korean J. Chem. Eng.*, **34**, 2459 (2017).
13. Q. Zhang, M. Zhou, X. Liu and B. Zhang, *J. Membr. Sci.*, **636**, 119612 (2021).
14. S. M. A. Ahmadi, T. Mohammadi and N. Azizi, *J. Appl. Polym. Sci.*, **138**, 50749 (2021).
15. L. Wang, Y. Li, S. Li, P. Ji and C. Jiang, *J. Energy Chem.*, **23**, 717 (2014).
16. S. M. A. Ahmadi, T. Mohammadi and N. Azizi, *Korean J. Chem. Eng.*, **38**, 104 (2021).
17. S. Feng, J. Ren, D. Zhao, H. Li, K. Hua, X. Li and M. Deng, *J. Appl. Polym. Sci.*, **136**, 47620 (2019).
18. S. Feng, J. Ren, K. Hua, H. Li, X. Ren and M. Deng, *Sep. Purif. Technol.*, **116**, 25 (2013).
19. I. Salahshoori, I. Cacciotti, A. Seyfaee and A. Babapoor, *J. Polym. Res.*, **28**, 223 (2021).
20. J. Qiu, J.-M. Zheng and K.-V. Peinemann, *Macromolecules*, **40**, 3213 (2007).
21. A. Gonzalez, M. Iriarte, P. Iriondo and J. Iruin, *Polymer*, **43**, 6205 (2002).
22. N. Azizi, M. R. Hojjati and M. M. Zarei, *Silicon*, **10**, 1461 (2018).
23. R. He, S. Cong, S. Xu, S. Han, H. Guo, Z. Liang, J. Wang and Y. Zhang, *J. Membr. Sci.*, **624**, 119081 (2021).
24. L.-E. José Cirilo Ignacio, L. Ant, S. Karl and B. Emilio, *Open J. Polym. Chem.*, **2012**, 63 (2012).
25. A. H. Ruhaimi, M. A. A. Aziz and A. A. Jalil, *J. CO_2 Util.*, **43**, 101357 (2021).
26. Y. Hu, Y. Guo, J. Sun, H. Li and W. Liu, *J. Mater. Chem. A*, **7**, 20103 (2019).
27. A. Atash Jameh, T. Mohammadi and O. Bakhtiari, *Sep. Purif. Technol.*, **231**, 115900 (2020).
28. J. Hou, X. Li, Y. Zhao, R. Guo and W. Tian, *ACS Appl. Nano Mater.*, **5**, 15310 (2022).
29. T. Khosravi and M. Omidkhah, *J. Energy Chem.*, **26**, 530 (2017).
30. M. H. Jazebizadeh and S. Khazraei, *Silicon*, **9**, 775 (2017).
31. S. Wang, Y. Liu, S. Huang, H. Wu, Y. Li, Z. Tian and Z. Jiang, *J. Membr. Sci.*, **460**, 62 (2014).
32. A. Mahmoudi, M. Asghari and V. Zargar, *J. Ind. Eng. Chem.*, **23**, 238 (2015).
33. M. Isanejad, N. Azizi and T. Mohammadi, *J. Appl. Polym. Sci.*, **134**, 44531 (2017).
34. H. Hassanzadeh, R. Abedini and M. Ghorbani, *Ind. Eng. Chem. Res.*, **61**, 13669 (2022).
35. X. Lv, X. Li, L. Huang, S. Ding, Y. Lv and J. Zhang, *Korean J. Chem. Eng.*, **39**, 475 (2022).
36. N. Azizi, T. Mohammadi and R. M. Behbahani, *J. Nat. Gas Sci. Eng.*, **37**, 39 (2017).
37. N. Azizi, H. R. Mahdavi, M. Isanejad and T. Mohammadi, *J. Polym. Res.*, **24**, 141 (2017).
38. L. Yu, W. Xue, L. Cui, W. Xing, X. Cao and H. Li, *Int. J. Biol. Macromol.*, **64**, 233 (2014).
39. A. Ghadimi, T. Mohammadi and N. Kasiri, *Ind. Eng. Chem. Res.*, **53**, 17476 (2014).
40. H. R. Mahdavi, N. Azizi and T. Mohammadi, *J. Polym. Res.*, **24**, (2017).
41. A. Ghadimi, M. Amirilargani, T. Mohammadi, N. Kasiri and B. Sadatnia, *J. Membr. Sci.*, **458**, 14 (2014).
42. S. Hassanajili, M. Khademi and P. Keshavarz, *J. Membr. Sci.*, **453**, 369 (2014).
43. M. Isanejad and T. Mohammadi, *Mater. Chem. Phys.*, **205**, 303 (2018).
44. N. Azizi, T. Mohammadi and R. M. Behbahani, *J. Energy Chem.*, **26**, 454 (2017).
45. N. Azizi, T. Mohammadi and R. Mosayebi Behbahani, *Chem. Eng. Res. Des.*, **117**, 177 (2017).
46. A. F. Ismail, K. C. Khulbe and T. Matsuura, Gas Separation Membrane Materials and Structures, Gas Separation Membranes: Polymeric and Inorganic, Springer, Switzerland, 37 (2015).
47. V. Nafisi and M.-B. Hägg, *J. Membr. Sci.*, **459**, 244 (2014).
48. R. Surya Murali, A. F. Ismail, M. A. Rahman and S. Sridhar, *Sep. Purif. Technol.*, **129**, 1 (2014).
49. D. Zhao, J. Ren, H. Li, X. Li and M. Deng, *J. Membr. Sci.*, **467**, 41 (2014).
50. D. Turnbull and M. H. Cohen, *J. Chem. Phys.*, **52**, 3038 (1970).
51. Y. Qiu, J. Ren, D. Zhao, H. Li and M. Deng, *J. Energy Chem.*, **25**, 122 (2016).
52. J. H. Kim and Y. M. Lee, *J. Membr. Sci.*, **193**, 209 (2001).
53. M. C. Choi, J. Y. Jung, H. S. Yeom and Y. W. Chang, *Polym. Eng. Sci.*, **53**, 982 (2013).
54. D. Dixon and A. Boyd, *Polym. Eng. Sci.*, **51**, 2203 (2011).
55. Y. Wang, J. Ren and M. Deng, *Sep. Purif. Technol.*, **77**, 46 (2011).
56. R. Surya Murali, K. Praveen Kumar, A. F. Ismail and S. Sridhar, *Micropor. Mesopor. Mater.*, **197**, 291 (2014).
57. C. S. Lee, E. Song, J. T. Park and J. H. Kim, *ACS Sustainable Chem. Eng.*, **9**, 11903 (2021).
58. A. Car, C. Stropnik, W. Yave and K.-V. Peinemann, *J. Membr. Sci.*, **307**, 88 (2008).
59. H. Rabiee, S. Meshkat Alsadat, M. Soltanieh, S. A. Mousavi and A. Ghadimi, *J. Ind. Eng. Chem.*, **27**, 223 (2015).
60. M. Rezakazemi, A. Vatani and T. Mohammadi, *RSC Adv.*, **5**, 82460 (2015).
61. Y. Yampolskii and B. Freeman, *Membrane gas separation*, Wiley Online Library (2010).

62. H. Sanaeepur, R. Ahmadi, A. E. Amooghin and D. Ghanbari, *J. Membr. Sci.*, **573**, 234 (2019).
63. S. T. Matteucci, Gas transport properties of reverse selective nanocomposite materials, The University of Texas at Austin, Ann Arbor (2007).
64. S. Matteucci, V. A. Kusuma, D. Sanders, S. Swinnea and B. D. Freeman, *J. Membr. Sci.*, **307**, 196 (2008).
65. A. Shariati, M. Omidkhah and M. Z. Pedram, *Chem. Eng. Res. Des.*, **90**, 563 (2012).
66. M. Sadeghi, M. Mehdi Talakesh, B. Ghalei and M. Shafiei, *J. Membr. Sci.*, **427**, 21 (2013).
67. M. M. Rahman, V. Filiz, S. Shishatskiy, C. Abetz, S. Neumann, S. Bolmer, M. M. Khan and V. Abetz, *J. Membr. Sci.*, **437**, 286 (2013).
68. H. Lin and B. D. Freeman, *Macromolecules*, **38**, 8394 (2005).
69. L. M. Robeson, *J. Membr. Sci.*, **320**, 390 (2008).
70. L. M. Robeson, *J. Membr. Sci.*, **62**, 165 (1991).
71. F. Dorosti and A. Alizadehdakhel, *Chem. Eng. Res. Des.*, **136**, 119 (2018).